Supporting Information

Monitoring the Crystal Structure and the Electrochemical Properties of $Na_3(VO)_2(PO_4)_2F$ through Fe^{3+}-Substitution

Long H.B. Nguyen [a,b,e], Jacob Olchowka [a,e,f], Stéphanie Belin [c], Paula Sanz Camacho [a], Mathieu Duttine [a], Antonella Iadecola [e], François Fauth [d], Dany Carlier [a,e,f], Christian Masquelier [b,e,f], Laurence Croguennec [a,e,f] *

[a] CNRS, Univ. Bordeaux, Bordeaux INP, ICMCB UMR 5026, F-33600, Pessac, France.

[b] Laboratoire de Réactivité et de Chimie des Solides, CNRS-UMR #7314, Université de Picardie Jules Verne, F-80039 Amiens Cedex 1, France.

[c] SOLEIL Synchrotron, F-91192 Gif-sur-Yvette, France.

[d] CELLS-ALBA synchrotron, E-08290 Cerdanyola del Vallès, Barcelona, Spain.

[e] RS2E, Réseau Français sur le Stockage Electrochimique de l'Energie, FR CNRS 3459, F-80039 Amiens Cedex 1, France.

[f] ALISTORE-ERI European Research Institute, FR CNRS 3104, Amiens, F-80039 Cedex 1, France.

* Corresponding author: L. Croguennec (Laurence.Croguennec@icmcb.cnrs.fr)

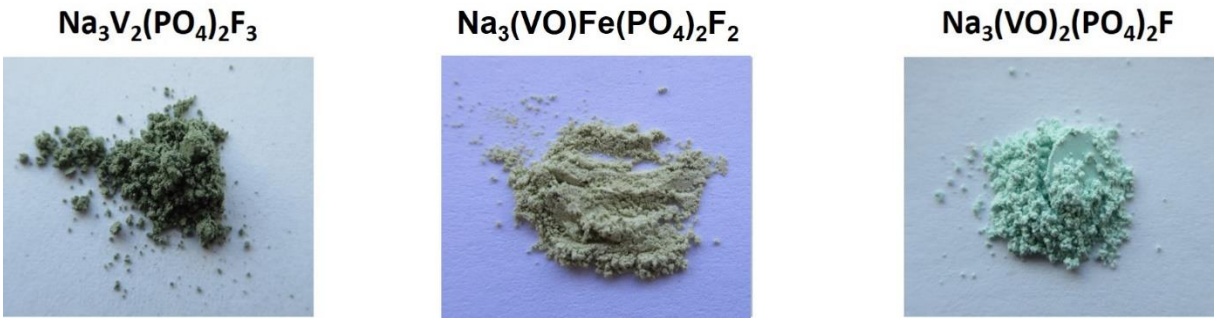

Figure S1: A comparison of the color of the three samples: $Na_3V_2(PO_4)_2F_3$, $Na_3(VO)Fe(PO_4)_2F_2$, and $Na_3(VO)_2(PO_4)_2F$.

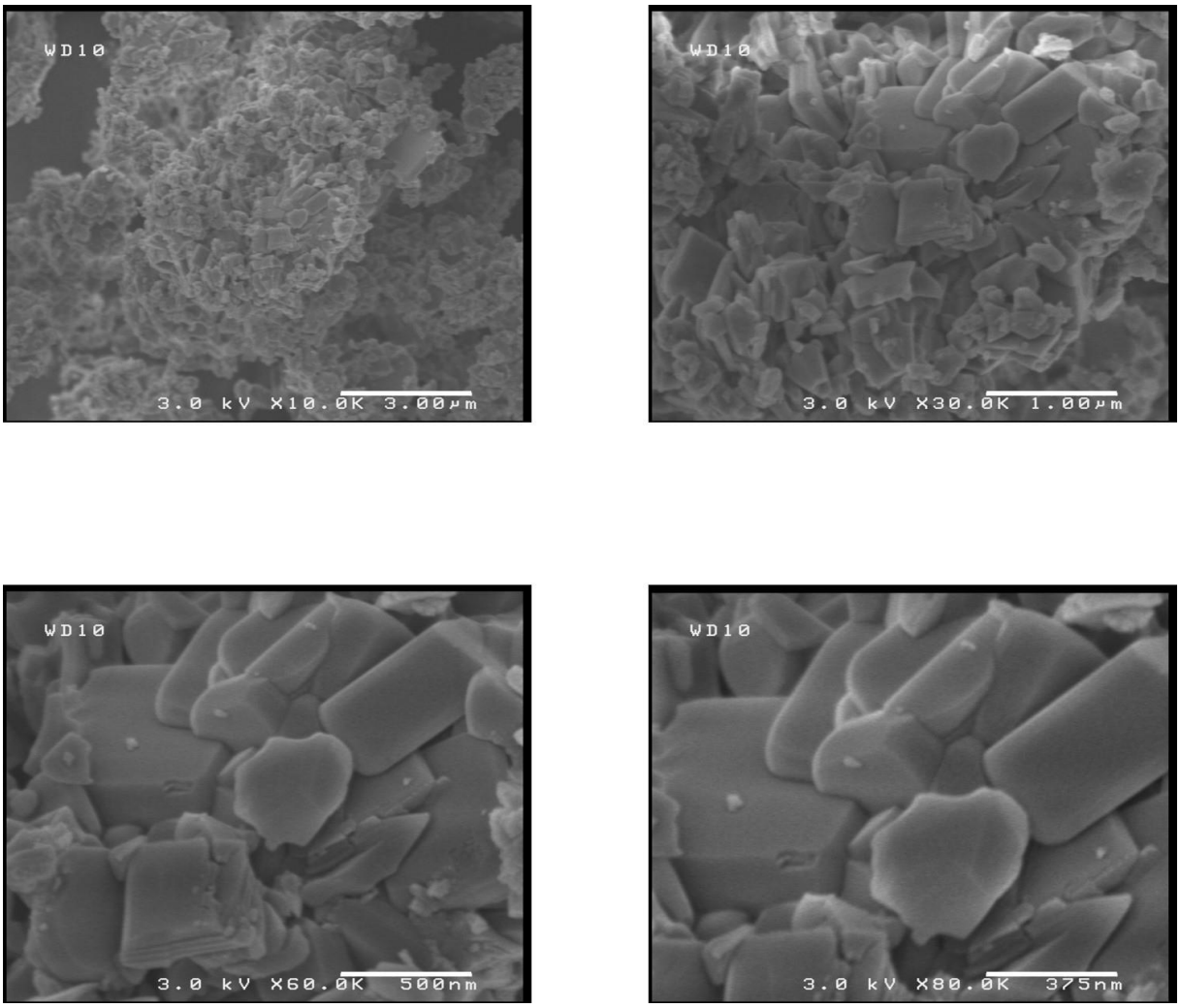

Figure S2: SEM images of $Na_3(VO)Fe(PO_4)_2F_2$ at different magnifications.

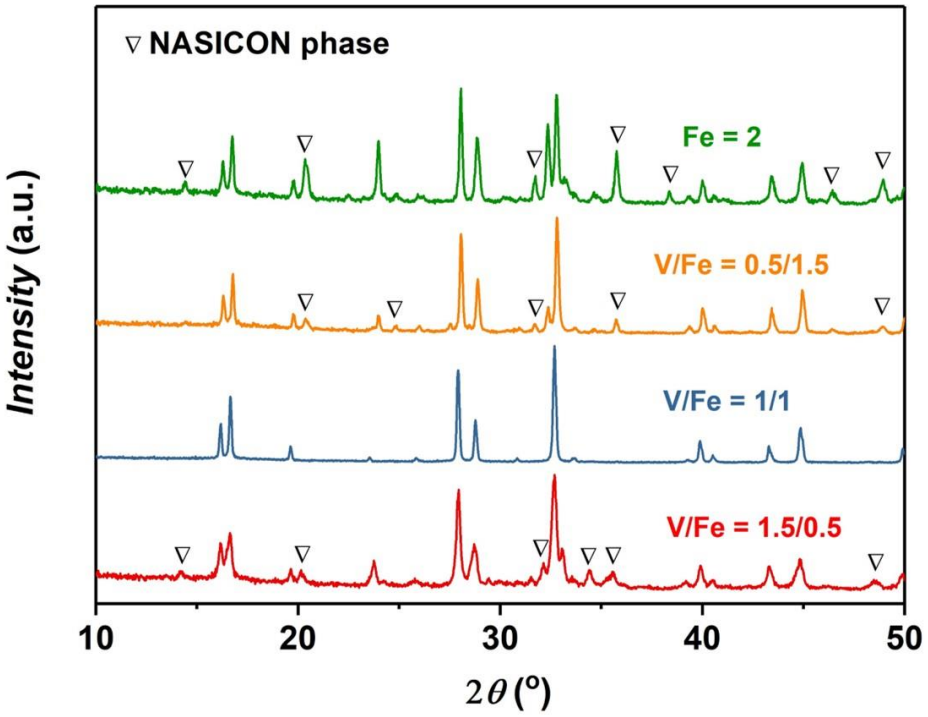

Figure S3: XRPD patterns collected using the Cu $K_{\alpha 1,2}$ radiation for the products obtained for different V: Fe precursor ratios. A calcination process was performed at 550°C during 3h. A pure phase was obtained when the initial V: Fe ratio was equal to 1: 1. In other cases, mixtures of NVPF- and NASICON-type phases were obtained.

We varied the initial V: Fe molar ratio from 1.5:0.5 to Fe-only in order to synthesize the Fe^{3+}-substituted $Na_3(VO)_2(PO_4)_2F$ phases with different V: Fe stoichiometries. The syntheses were performed in the same conditions as those reported for $Na_3(VO)Fe(PO_4)_2F_2$. A black powder was obtained for V: Fe = 1.5: 0.5 while a slightly yellow powder was recovered for V: Fe = 0.5: 1.5. The XRPD patterns of these phases revealed that the obtained powders were not well crystallized, as highlighted by the broadening of the diffraction lines and thus by the low signal-to-noise ratio. Furthermore, the final products were shown to be mixtures of NVPF-like and NASICON-like phases.

When only $Fe(NO_3)_3.9H_2O$ was used as transition metal precursor, $Na_3Fe_2(PO_4)_2F_3$ was obtained as a red powder, but the phase was not pure. We also varied the thermal treatment

conditions, *i.e*. temperature as well as the calcination dwelling time. Nevertheless, no pure and well crystallized phase was successfully obtained.

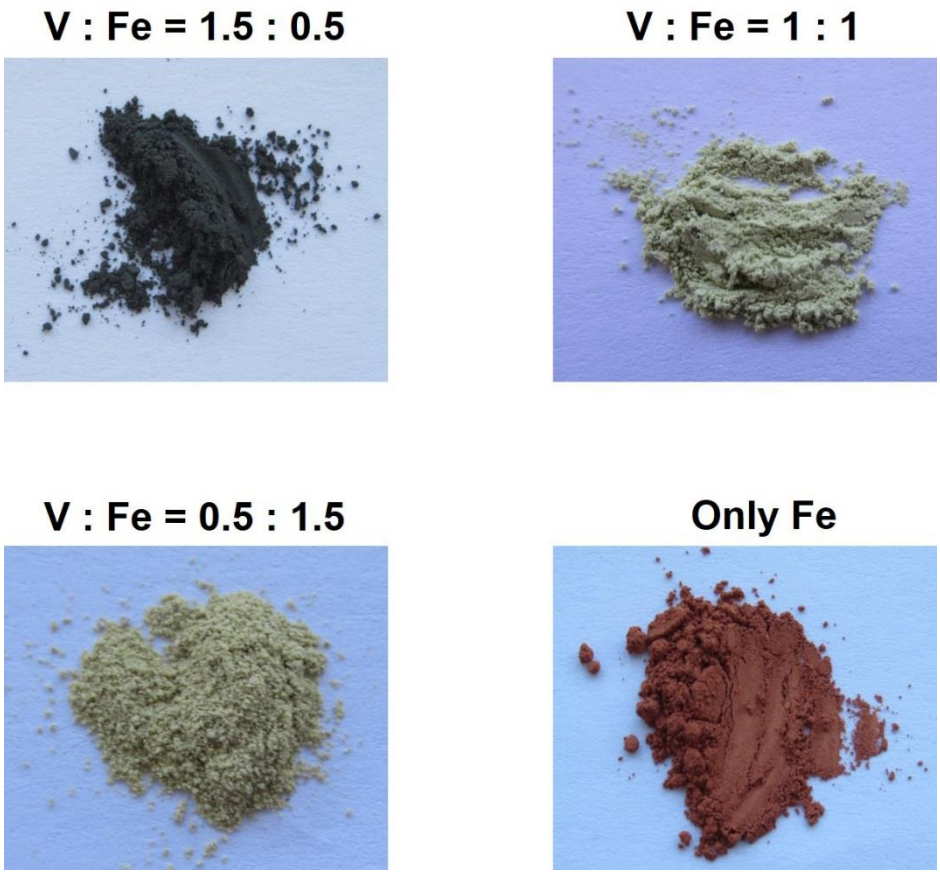

Figure S4: Color of the powders obtained for different V: Fe ratios after a calcination at 550°C under Ar atmosphere during 3h.

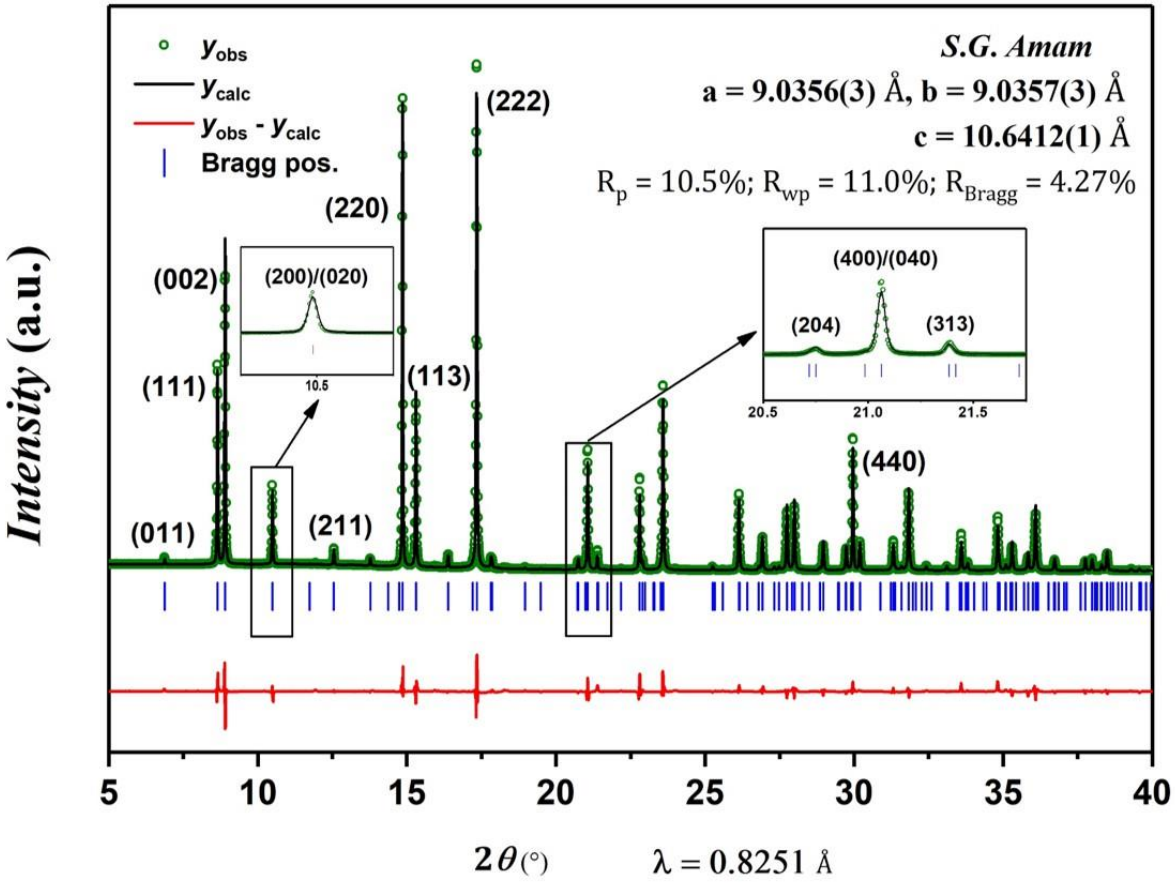

Figure S5: Result of the Rietveld refinement performed in the *Amam* space group on the synchrotron X-ray powder diffraction data recorded on the $Na_3(VO)Fe(PO_4)_2F_2$ phase.

Table S1: A comparison of the interatomic distances in $Na_3(VO)Fe(PO_4)_2F_2$ obtained from Rietveld refinements by considering two structural descriptions: *Amam* and $P4_2/mnm$ space groups.

Amam		***P4₂/mnm***	
	Interatomic distances (Å)		**Interatomic distances (Å)**
P(1)-O(1)	1.582(6) x 2	**P(1)-O(1)**	1.529(6) x **4**
P(1)-O(2)	1.490(7) x 2	**P(2)-O(2)**	1.595(8) x **2**
		P(2)-O(3)	1.493(8) x **2**
V/Fe-O(1)	2.001(7) x 2	**V(1)-O(1)**	2.013(6) x **2**
V/Fe-O(2)	1.993(7) x 2	**V(1)-O(2)**	1.954(6)
		V(1)-O(3)	1.983(6)
V/Fe-F(1)	2.040(1)	**V(1)-F(1)**	2.040(1)
V/Fe-F(2)/O(3)	1.802(4)	**V(1)-F(2)/O(4)**	1.795(1)

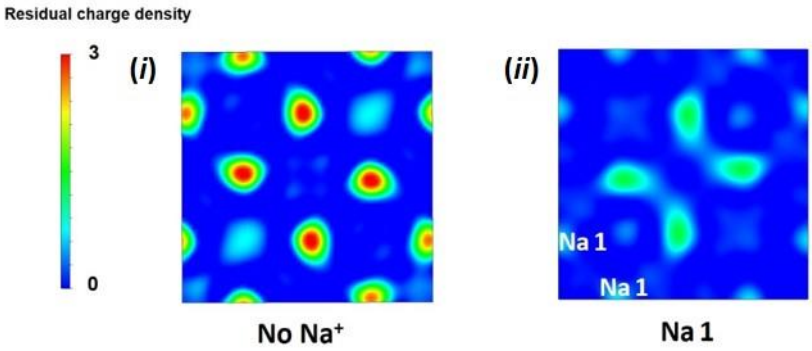

Figure S6: Calculated Fourier difference maps with the residual charge density ranging from 0 - 3 for (*i*) (VO)Fe(PO_4)$_2F_2$ framework without the presence of Na^+ and (*ii*) (VO)Fe(PO_4)$_2F_2$ framework with the presence of Na1

Rietveld refinement was performed on the SXRPD data recorded on Na_3(VO)Fe(PO_4)$_2F_2$ by considering only (VO)Fe(PO_4)$_2F_2$ framework described in the $P4_2/mnm$ space group. Fourier difference maps were calculated once the refinement converged, the residual charge density observed on the maps indicated the positions of Na^+ ions in the structure.

By taking into account only the (VO)Fe(PO_4)$_2F_2$ framework, the calculated Fourier difference map shows huge residual charge densities. By placing consecutively Na1 and Na2 sites into the structure, the residual charge density is greatly decreased. Finally, it is fully minimized by considering three different Na sites.

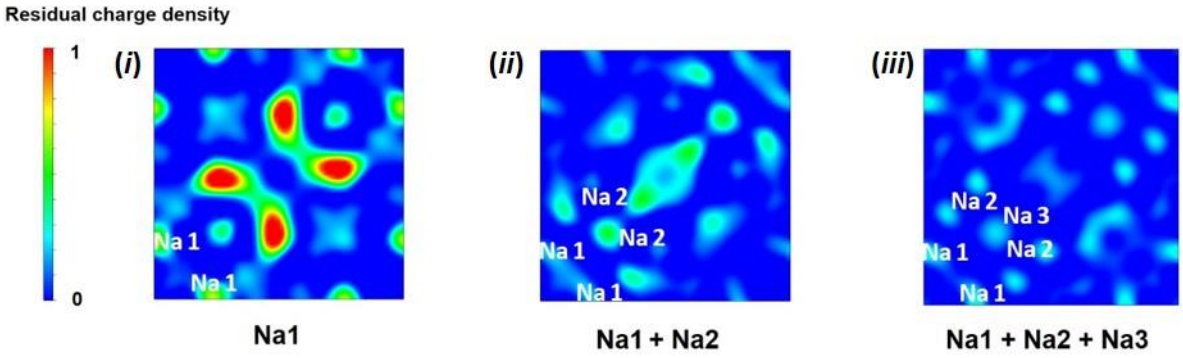

Figure S7: Calculated Fourier difference maps with the residual charge density ranging from 0 - 1 for (*i*) (VO)Fe(PO_4)$_2F_2$ framework with the presence of Na1, (*ii*) (VO)Fe(PO_4)$_2F_2$ framework with the presence of Na1 and Na2, and (*iii*) (VO)Fe(PO_4)$_2F_2$ framework with the presence of Na1, Na2 and Na3

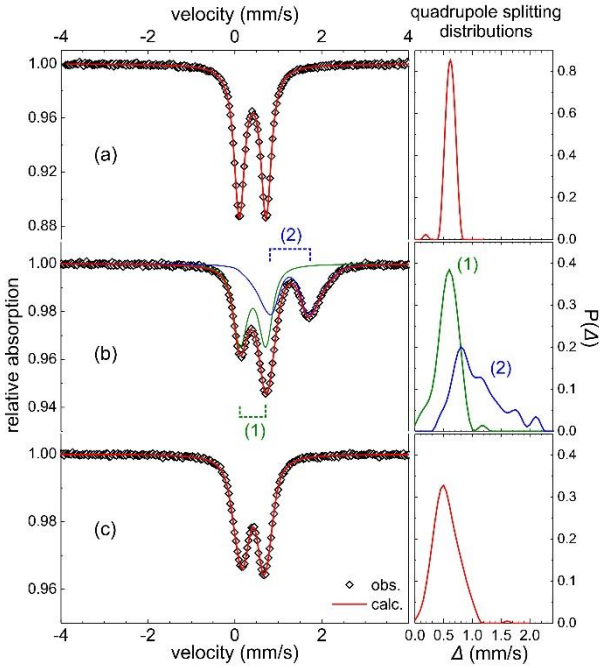

Figure S8: Room temperature ^{57}Fe Mössbauer spectra of (*a*) the pristine material $Na_3(VO)Fe(PO_4)_2F_2$, (*b*) the material recovered after Na^+ intercalation in $Na_3(VO)Fe(PO_4)_2F_2$ by discharging the cell down to 1.5 V vs. Na^+/Na. The ^{57}Fe Mössbauer spectrum recorded for this composition shows the presence of Fe^{3+} and Fe^{2+} with their contributions marked as (1) and (2), respectively, (*c*) the material recovered after the Na^+ de-intercalation from $Na_3(VO)Fe(PO_4)_2F_2$ by charging the cell up to 5.0 V vs. Na^+/Na. The asymmetry of the last spectrum (*c*) was due to texture effects (confirmed by a measurement performed at the so-called "magic angle") and was taken into account in the fitting procedure. All sub-spectra were calculated using a distribution of the quadrupole splitting (Δ) hyperfine parameter (right panel).

Table S2: Refined room temperature ^{57}Fe Mössbauer hyperfine parameters for (*i*) the pristine material $Na_3(VO)Fe(PO_4)_2F_2$, (*ii*) the material recovered after Na^+ intercalation in $Na_3(VO)Fe(PO_4)_2F_2$ by discharging the cell down to 1.5 V vs. Na^+/Na and (*iii*) the material recovered after Na^+ de-intercalation from $Na_3(VO)Fe(PO_4)_2F_2$ by charging the cell up to 5.0 V vs. Na^+/Na. (δ isomer shift in respect to α-Fe, Δ quadrupole splitting, Γ Lorentzian line width and A relative area). (*) mean value of the Δ distribution.

Sample	*sub.*	δ (mm/s)	Δ (mm/s)	Γ (mm/s)	A (%)	assignment
(*i*) Pristine	QD1	0.41(1)	0.61(*)	0.25(-)	100	HS-Fe^{3+}
(*ii*) Intercalated (1.5 V)	QD1	0.42(1)	0.57(*)	0.25(-)	53(3)	HS-Fe^{3+}
	QD2	1.26(1)	1.08(*)	0.25(-)	47(3)	HS-Fe^{2+}
(*iii*) De-intercalated (5 V)	QD1	0.42(1)	0.55(*)	0.25(-)	100	HS-Fe^{3+}

In order to quantify the Fermi contact interaction, the VASP code can compute the hyperfine coupling contact by considering the contribution of valence and core electrons:

$$A_{iso} = \frac{2}{3} \frac{\mu_0 \gamma_e \gamma_N}{\langle S_N \rangle} \int \delta_T(r) \rho_s(r + R_I) dr \qquad (1)$$

where ρ_s is the difference of the population between the spin-up and spin-down energy levels at a specific nucleus where the hyperfine coupling constant is calculated and ρ_s is usually known as "electronic spin density", μ_0 is the magnetic susceptibility of free space, γ_e is the electronic gyromagnetic ratio, γ_N is the nuclear gyromagnetic ratio of the probed nucleus, R_I is the nucleus radius, and $\langle S_N \rangle$ is the expected value of the *z*-component of the total electron spin. $\delta_T(r)$ is a smeared out of δ function, as described in the literature.

The spin density surrounding the nucleus of interest ($\rho^i(0)$) can further be calculated from the A_{iso} value by the following equation:

$$\rho^i(0) = \frac{A_{iso} S(Tot)}{\gamma_N} \qquad (2)$$

with S(Tot) is the total magnetic moment in the unit cell, γ_N is the nuclear gyromagnetic ratio of the nuclear of interest, and A_{iso} is the hyperfine coupling constant as described in equation (1).

The isotropic shift of a specific nucleus due to Fermi contact can then be quantified from the electron spin density:

$$\delta^i_{iso} = \frac{1}{3SN_A} \rho^i(0) \chi_M(T) \qquad (3)$$

where S is the spin quantum number of the paramagnetic ion, $\rho^i(0)$ is the computed spin density on the *i* nucleus, and $\chi_M(T)$ is the molar magnetic susceptibility at the temperature at which the NMR spectrum was recorded.

The following nuclear gyromagnetic ratio ($MHz \cdot T^{-1}$) were used for the calculations: 1.382 (^{57}Fe), 17.2538 (^{31}P), 11.271 (^{23}Na), 40.078 (^{19}F), and 5.775 (^{17}O). The Curie temperature was assumed to be 0K for all compounds and the theoretical value of molar magnetic susceptibility calculated by Curie law was used for the Fermi contact shift calculation. The temperature (*T*) was chosen to be 320K, which is the approximate temperature inside the rotor at a spinning rate of 30 *k*Hz.

In order to understand the origin of the paramagnetic resonances observed on the ^{31}P NMR spectrum of $Na_3(VO)Fe(PO_4)_2F_2$, we performed DFT calculations with the plot of spin distribution map for the phase $Na_3Fe_2(PO_4)_2F_3$ and compared it to those of $Na_3(VO)_2(PO_4)_2F$.

The crystal structure of $Na_3Fe_2(PO_4)_2F_3$ was reported by Le Meins *et al*., however it contains six partially occupied Na sites,[1] which cannot be taken into account in the DFT calculations. Furthermore, in this study, we only want to investigate the electron spin transfer between Fe^{3+} and its neighboring phosphorus nuclei, which is not influenced by the positions of Na^+ ions in the diffusion channels. An approximate $Na_3Fe_2(PO_4)_2F_3$ input model was constructed based on the crystal structure of $Na_3V_2(PO_4)_2F_3$ by replacing all vanadium atoms in the unit cell by iron. The $Na_3Fe_2(PO_4)_2F_3$ input model was then relaxed by using the GGA method until the system reached it minimum energy. The spin density on each nucleus in the crystal structure as well as the spin distribution map were calculated on the optimized structure.

Table S3: A comparison of the cell parameters between the input model and the optimized structure

	Input model	Optimized structure by GGA
***a* (Å)**	9.029	9.148
***b* (Å)**	9.024	9.196
***c* (Å)**	10.747	10.778
α	90°	90°
β	90°	90°
γ	90°	90°

The calculated spin distribution map shows that each phosphorus nucleus in the unit cell is surrounded by four Fe^{3+} ions and all these Fe^{3+} possess five spin-up electrons. Thanks to the orbital overlap between 3*d* orbitals of Fe^{3+} and hybridized orbital sp^3 of phosphorus, the spin electrons on Fe^{3+} can be transferred on phosphorus site. The presence of the high density of the electron spin close to the phosphorus center will lead to a strong electron - nuclear spin interaction (Fermi contact), resulting in the high paramagnetic shift on the ^{31}P NMR spectrum.

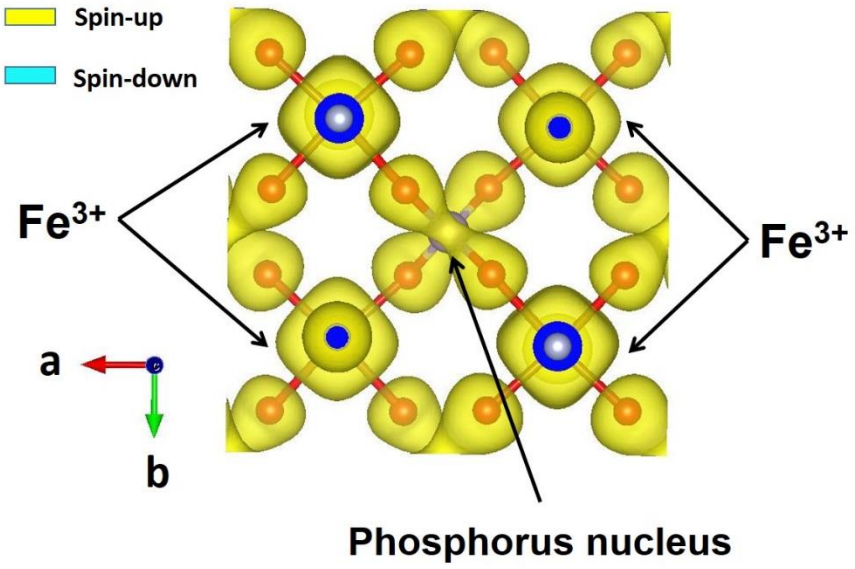

Figure S9: Electron spin density calculated at an iso-surface value of $2 \cdot 10^{-3}$ electron·Å^{-1} for $Na_3Fe_2(PO_4)_2F_3$. The 'spin-up' electrons are represented by the yellow region while the 'spin down' electrons are represented in blue.

The theoretical paramagnetic shift for this $P(OFe^{3+})_4$ local environment is ~ 8400 ppm. As we have recently demonstrated that there is no Fermi contact between V^{4+} and phosphorus nuclei in this structural framework, the magnitude of the Fermi contact will depend only on the presence of Fe^{3+} ions in the proximity of the phosphorus nucleus. Each Fe^{3+} will contribute to a shift value of ~ 2100 ppm while there is no contribution of V^{4+} to the paramagnetic shift of ^{31}P. In a recent work, we have reported that each V^{3+} ($3d^2$) in the proximity of a Phosphorus atom in this structural framework will contribute to a paramagnetic shift of ~ 1500 ppm due to the Fermi contact.[3] In the case of Fe^{3+}, due to the presence of more unpaired electrons ($3d^5$), each Fe^{3+} can contribute to a shift of ~ 2100 ppm.

Table S4 *:* The amplitude, chemical shift (δ), peak width, η value in the Pseudo-Voigt peak shape function, and the relative contribution of each ^{31}P NMR resonance recorded in the signal region of -100 to 200 ppm of $Na_3(VO)Fe(PO_4)_2F_2$.

	Amplitude	**δ (ppm)**	**Width (ppm)**	**η (Gaussian/Lorentzian)**	**Experimental contribution**	**Theoretical distribution**
n = 4	6337	139	18.7	0.2	6.6%	6.25%
n = 3	22955	105	18.6	0.2	23.8%	25%
n = 2	31220	69	22.4	0.2	32.3%	37.5%
n = 1	23818	33	19.9	0	24.6%	25%
n = 0	12338	-5	25.5	1.0*	12.7%	6.25%

The ^{31}P MAS NMR signals in Figure 4a were fit using the DMfit program. The theoretical distribution value was calculated using the binomial distribution equation by considering that V^{4+} and Fe^{3+} ions are randomly distributed in the four second octahedral units of the $P(OV^{4+})_4$ local environment (Figure 4a). The *n* value (*n* = 0, 1, 2, 3, and 4) indicates the number of Fe^{3+} in the second transition metal sites with respect to the phosphorus, $P(OV^{4+}{-}F{-}(V^{4+})_{4-n}(Fe^{3+})_n$. The Pseudo-Voigt function is defined as a convolution of the Gaussian and the Lorentzian peak shape function: Pseudo-Voigt = (1 - η) Gaussian + η Lorentzian.

* The intensity of the peak with *n* = 0 was greatly influenced by the presence of the background at $\delta \leq$ -50 ppm, hence a pure Lorentzian function was used for the peak fitting and its η value was not refined.

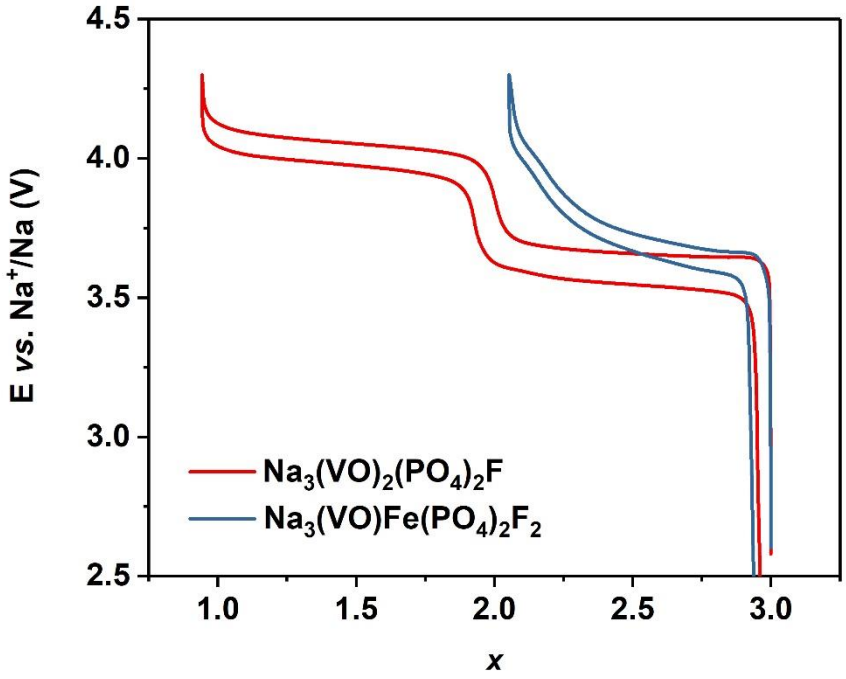

Figure S10: Comparison of the electrochemical properties between $Na_3(VO)_2(PO_4)_2F$ and $Na_3(VO)Fe(PO_4)_2F_2$.

The electrodes were prepared by the same method for the two materials, *i.e.* mixing the active material, carbon black and the PTFE binder in the mass ratio of 80: 10: 10 (by wt.%). The electrodes were then cycled in a half-cell vs. Na metal, in the potential range of 2.5 - 4.3 V at the cycling rate of *C*/10 per Na^+. When cycled in the same conditions, the polarization observed for the Na//$Na_3(VO)Fe(PO_4)_2F_2$ half-cell is smaller than that of Na//$Na_3(VO)_2(PO_4)_2F$. However, only one Na^+ ion can be extracted from $Na_3(VO)Fe(PO_4)_2F_2$, while two Na^+ ions can be de-intercalated from $Na_3(VO)_2(PO_4)_2F$.

$Na_3(VO)_2(PO_4)_2F$ **$Na_3(VO)Fe(PO_4)_2F_2$**

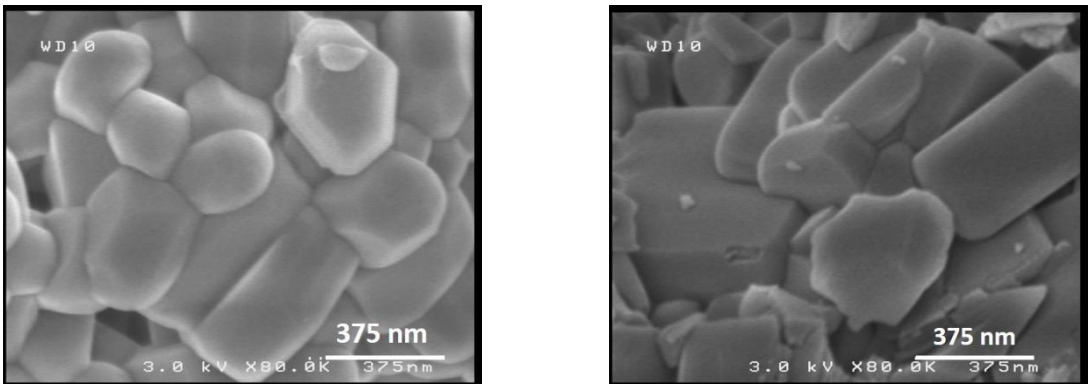

Figure S11: A comparison of the primary particles' size between $Na_3(VO)_2(PO_4)_2F$ and $Na_3(VO)Fe(PO_4)_2F_2$.

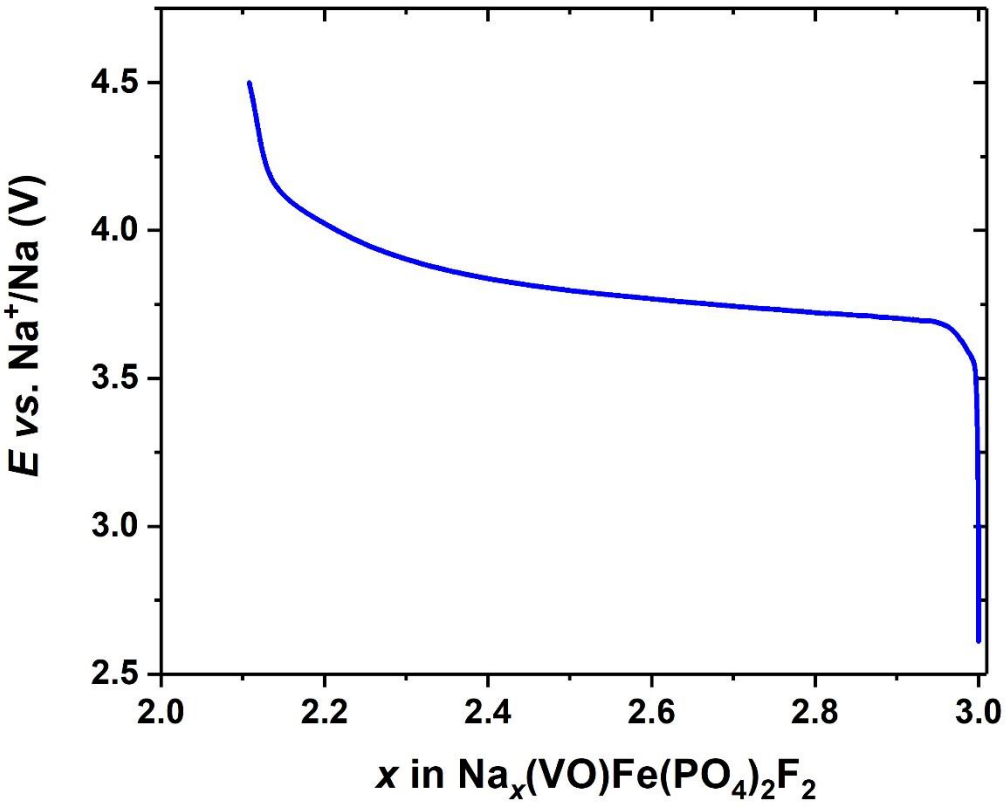

Figure S12*:* The electrochemical profile of a Na//$Na_3(VO)Fe(PO_4)_2F_2$ half-cell used in the operando synchrotron X-ray powder diffraction experiment. The cell was cycled at *C*/10 per Na^+ in the potential range of 2.5 - 4.5 V vs. Na^+/Na. The positive electrode was composed of $Na_3(VO)Fe(PO_4)_2F_2$: carbon black: PTFE in the ratio of 80: 10: 10 (by wt.%).

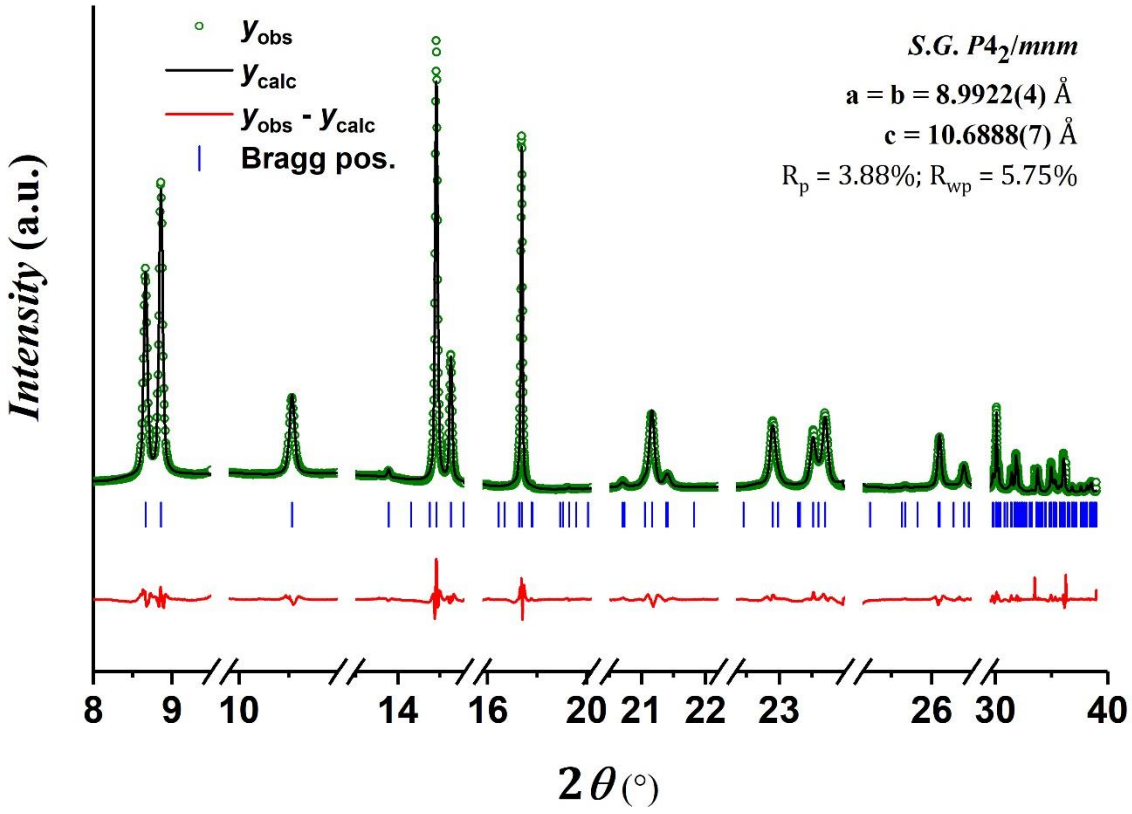

Figure S13: Le Bail fit of $Na_{2.54}(VO)Fe(PO_4)_2F_2$ recorded at pattern #25 on a $Na//Na_3(VO)Fe(PO_4)_2F_2$ half-cell at λ = 0.8251 Å. The regions corresponding to the diffraction lines of Na metal, Be window, and Al current collector were excluded from the profile matching. The Le Bail fit was done considering the structural description in the tetragonal unit cell ($P4_2/mnm$ space group).

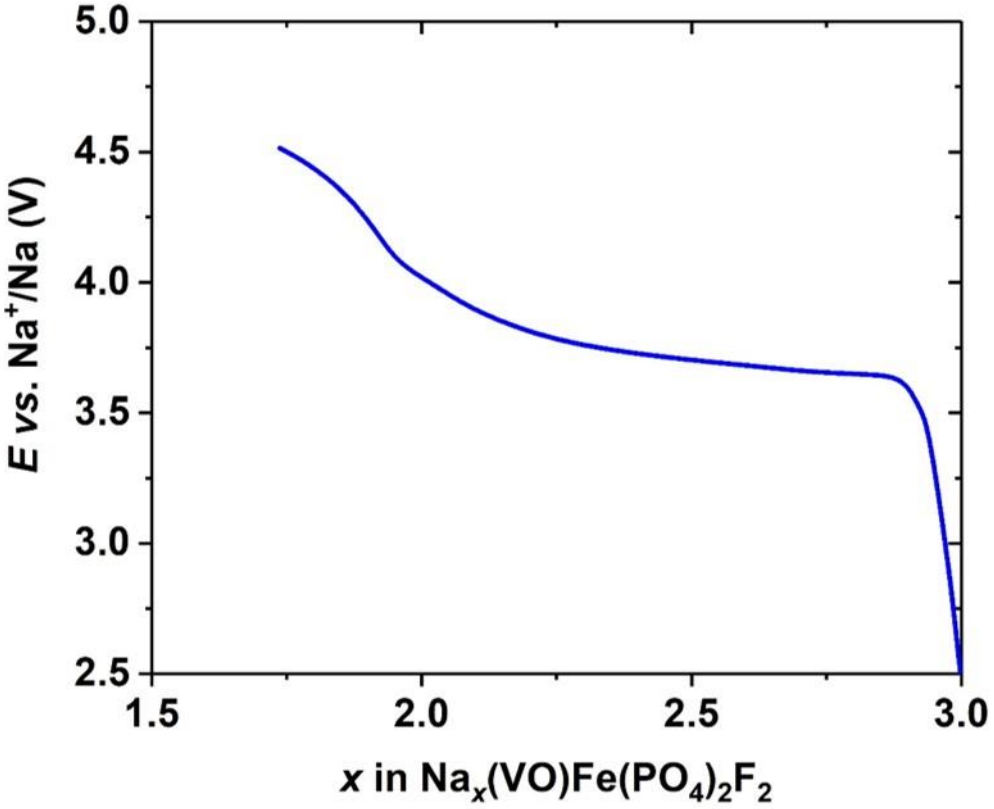

Figure S14: The electrochemical profile of a Na//$Na_3(VO)Fe(PO_4)_2F_2$ half-cell used for the *operando* synchrotron X-ray absorption at Vanadium K-edge experiment. The cell was cycled at *C*/10 per Na^+ in the potential range of 2.5 - 4.5 V vs. Na^+/Na. The positive electrode was composed of $Na_3(VO)Fe(PO_4)_2F_2$: carbon black: PTFE in the ratio of 30: 60: 10 (by wt.%). The larger amount of carbon black was added to the electrode composite in order to dilute the active material in the carbon matrix.

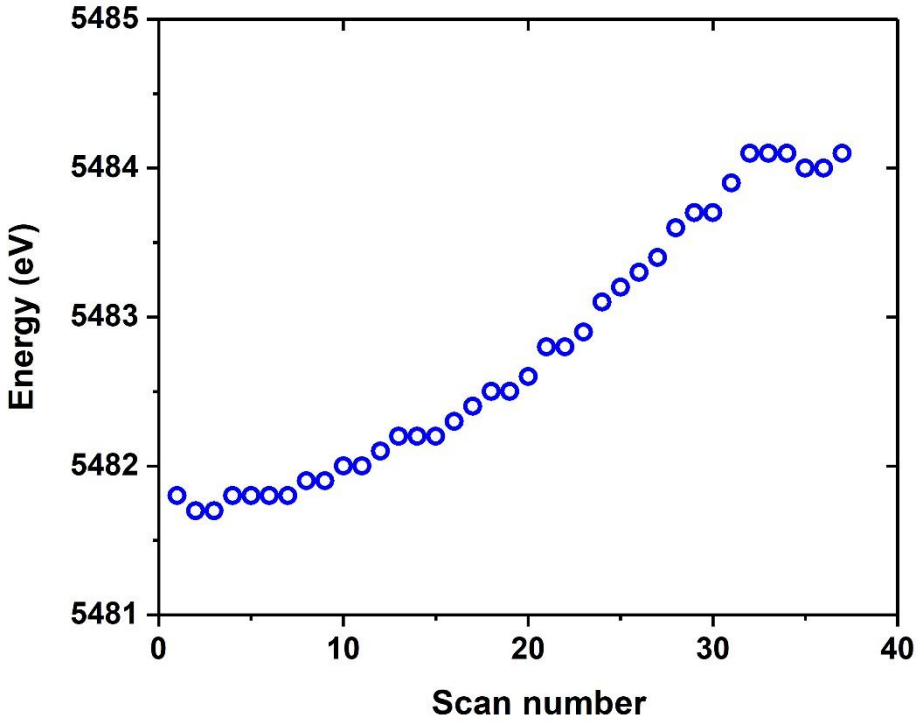

Figure S15: The evolution of the energy of the absorption edge (taken at the normalized intensity = 0.8) of the Vanadium K edge XANES spectra recorded *operando* a Na//$Na_3(VO)Fe(PO_4)_2F_2$ half-cell.

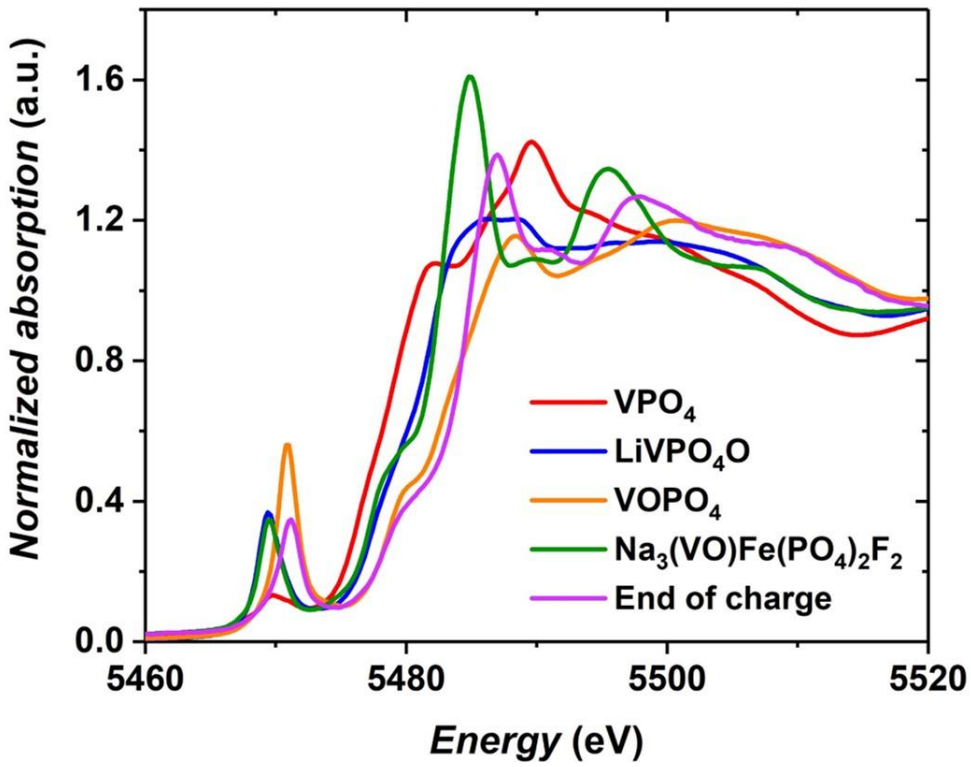

Figure S16: Vanadium K-edge XANES spectra recorded on a Na//$Na_3(VO)Fe(PO_4)_2F_2$ half-cell at the initial state and at the end of charge. The spectra of $V^{3+}PO_4$, $LiV^{4+}PO_4O$ and $V^{5+}OPO_4$ were used as external references to determine the oxidation state of Vanadium.

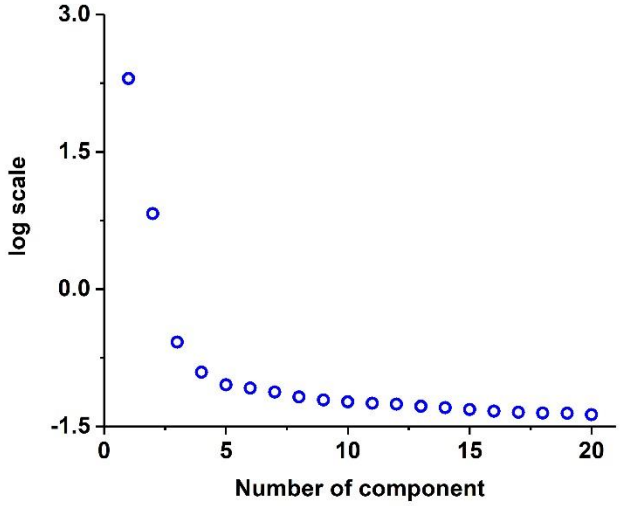

Figure S17: Variance plot of PCA for the operando XANES data.

The spectra reconstruction was done using the 'Pure' and 'Evolving Factor Analysis' (EFA) methods. In order to produce the chemically and physically meaningful results, the concentration profile of the principal components was constructed by applying the following constraints: (*i*) non-negative concentration value, (*ii*) unimodality (the concentration of each principal component can reach the maximum value only once), and (*iii*) closure (the sum of the concentration of all the components must be equal to one).[4] The variance plot obtained from the PCA analysis performed on the set of XAS spectra obtained *operando* indicates that two independent components are required to describe the whole system. The spectra reconstruction process using the 'Pure' and 'Evolving Factor Analysis' (EFA) methods gives the same results. The first reconstructed component is identical to the experimental spectrum of the pristine phase, $Na_3(VO)Fe(PO_4)_2F_2$, while the second component can be identified as being similar to the spectrum collected at the end of charge (Spectrum #37). All the other experimental XAS spectra can be calculated as a linear combination of these two reconstructed components. We can therefore conclude that the supposed solid solution mechanism is occurring also at the local scale. We also performed PCA analysis on the set of EXAFS spectra obtained *operando* and the output variance plot indicates, as for the XAS spectra, that two independent components are

necessary to interpret this system. These two independent components are also the initial and the final EXAFS spectra.

References:

[1] Le Meins, J.; Crosnier-Lopez, M.; Hemon-Ribaud, A.; Courbion, G.; Phase Transitions in the $Na_3M_2(PO_4)_2F_3$ Family (M = Al^{3+}, V^{3+}, Cr^{3+}, Fe^{3+}, Ga^{3+}) : Synthesis, Thermal, Structural, and Magnetic Studies. *J. Solid State Chem* **1999**, *148*, 260-277. DOI: 10.1006/jssc.1999.8447.

[2] Carlier, D.; Ménétrier, M.; Grey, C. P.; Delmas, C.; Ceder, G. Understanding the NMR Shifts in Paramagnetic Transition Metal Oxides Using Density Functional Theory Calculations. *Phys. Rev. B* **2003**, *67* (17), 174103(1)-174103(14). DOI: 10.1103/PhysRevB.67.174103.

[3] Nguyen, L. H. B.; Sanz Camacho, P.; Broux, T.; Masquelier, C.; Croguennec, L.; Carlier, D. ^{23}Na and ^{31}P Solid-State NMR: A Key Tool to Study Local Environments in $Na_3V_2(PO_4)_2F_{3-y}O_y$ ($0 \leq y \leq 2$) Materials. *In ECS 235th meeting*; **2019**, Abstract #544.

[4] Broux, T.; Bamine, T.; Simonelli, L.; Stievano, L.; Fauth, F.; Ménétrier, M.; Carlier, D.; Masquelier, C.; Croguennec, L. V^{IV} Disproportionation Upon Sodium Extraction From $Na_3V_2(PO_4)_2F_3$ Observed by Operando X-Ray Absorption Spectroscopy and Solid-State NMR. *J. Phys. Chem. C* **2017**, *121* (8), 4103–4111. DOI: 10.1021/acs.jpcc.6b11413.